

We are IntechOpen, the world's leading publisher of Open Access books Built by scientists, for scientists

6,900

Open access books available

185,000

International authors and editors

200M

Downloads

Our authors are among the

154

Countries delivered to

TOP 1%

most cited scientists

12.2%

Contributors from top 500 universities



WEB OF SCIENCE™

Selection of our books indexed in the Book Citation Index
in Web of Science™ Core Collection (BKCI)

Interested in publishing with us?
Contact book.department@intechopen.com

Numbers displayed above are based on latest data collected.
For more information visit www.intechopen.com



Fabrication of Yttrium-Doped Barium Zirconate for High Performance Protonic Ceramic Membranes

W. Grover Coors, Anthony Manerbino, David Martinefski and Sandrine Ricote

Additional information is available at the end of the chapter

<http://dx.doi.org/10.5772/61660>

Abstract

Barium zirconate has emerged as the leading candidate material for fabricating dense ceramic membranes for hydrogen separation. B-sites in the ABO_3 perovskite are acceptor-doped with a +3 cation – most commonly yttrium – charge-compensated by the formation of oxygen ion vacancies in the lattice. A minor fraction of B-sites can be filled with cerium to give $BaZr_{0.9-x}Ce_xY_{0.1}O_{3-d}$, $x \leq 0.2$. Upon hydration at elevated temperatures, weakly-bound protons are formed in the lattice. This produces a cubic perovskite ceramic proton conductor useful in diverse applications, such as protonic ceramic fuel cells, electrolyzers, and catalytic membrane reactors operating at temperatures between 600 and 800 °C. A necessary requirement for fabricating thin ceramic membranes for proton diffusion is to maximize grain size while eliminating percolating porosity. However, high-density, large-grained barium zirconate is a very difficult material to prepare by traditional powder sintering methods. This chapter describes a new methodology for making protonic ceramic membranes with large grains and virtually no residual porosity. This discovery has the potential to have a profound impact on energy conversion efficiency of the various membrane devices envisioned for the coming hydrogen energy economy.

Keywords: Protonic ceramics, Yttrium-doped barium zirconate, Hydrogen separation membranes, Solid-state reactive sintering

1. Introduction

Almost thirty-five years ago, Hiroyasu Iwahara reported high temperature proton conduction in strontium cerate perovskite [1]. In that same year, 1981, there was sufficient interest in the potential for proton conductors to warrant the first international symposium on solid-state proton conductors in Paris (SSPC-I). Interestingly, the possibility of proton transport in

perovskite ceramics was not widely recognized at this time. Several more years would pass before Iwahara's ground-breaking discoveries would be appreciated. Even at the fourth international symposium in 1989 (SSPC-IV) there was still general scepticism about proton conduction in perovskites [2]. It was not really until the early 1990's that the commercial importance of ceramic proton conductors sparked widespread interest among researchers. Acceptor-doped barium cerate soon became the model ceramic proton conductor. It exhibited high proton conductivity and was easy to fabricate into testable specimens, but before too long it was realized that barium cerate lacked the necessary chemical stability in the hot, moist, carbon dioxide-containing atmospheres of the typical use environment.

The first significant advancement into the modern era of ceramic proton conductors came from Klaus-Dieter Kreuer at the Max Planck Institute in 1999 [3] with the identification of the ceramic perovskite, barium zirconate, as a better candidate material due to its much greater chemical stability. However, unlike barium cerate, barium zirconate proved to be difficult to sinter by traditional ceramic methods. Some successes were achieved with solid solutions of barium cerate and zirconate [4], but still, it remained a challenge to make dense ceramic with more than 50% zirconium on B-sites, and any less than about 60% zirconium was still chemically unstable.

The second major breakthrough for barium zirconate ceramic processing came from Babilo and Haile at Caltech in 2005 [5] with the discovery of solid-state reactive sintering. Rather than using pre-reacted calcine powder, fully dense, large-grained barium zirconate ceramic membranes were fabricated directly from precursor powders with a small addition of NiO as a sintering additive. In this process, unreacted Ba from BaSO₄ and NiO form a binary eutectic glass that simultaneously promotes solid-state reaction and sintering. As the solid-state reaction proceeds, barium is extracted from the glass phase to take up A-sites in the more stable ABO₃ perovskite. Ultimately, the BaO-NiO glass becomes sufficiently barium deficient that the glass freezes out, leaving behind a thin film of NiO, which coats the grain boundaries [6].

In bulk ceramic material prepared this way, a small amount of NiO as a second phase has practically no impact, but when exposed to reducing atmosphere at high temperatures, the NiO nucleates to form Ni nanoparticles that decorate the dihedrals and grain facets. Under extreme operating conditions, depending on size and density, these nanoparticles can result in mechanical strain and fractures along grain boundaries. The formation of Ni nanoparticles hinders the use of membranes made by solid state reactive sintering in reducing atmosphere. Other sintering additives, which do not form nanoparticles, have been tried without much success. The eutectic temperature of BaO-NiO turns out to be almost perfect for the simultaneous solid-state reaction and liquid phase sintering process.

It became necessary to discover a way to remove the residual NiO from ceramic specimens after sintering. Such a process was discovered only last year, and will be described in what follows for barium zirconate-based materials with the nominal formula, BaZr_{0.9-x}Ce_xY_{0.1}O_{3-d'}, where $x \leq 0.2$. The term BZY will be used to refer to the ceramic formulation with more than 70 mol % Zr.

2. Background on barium zirconate

Over the past ten years, the perovskite ceramic, yttrium-doped barium zirconate has emerged as the most promising ceramic proton conductor [7-14]. In the ABO_3 structure, barium occupies A-sites and zirconium occupies B-sites. Yttrium (Y^{+3}) substitutes for Zr^{+4} on B-sites as an acceptor dopant that is compensated by the formation of oxygen ion vacancies. These vacancies on the oxygen ion sublattice have the remarkable property that water from the gas phase enters the oxygen vacancies at elevated temperatures, donating two quasi-free protons to the lattice (Eq 1) [15-18]. This behaviour requires just the right oxygen ion separation, and is unique to certain oxide ceramics, such as perovskites, and does not occur in more densely packed structures like yttrium-doped zirconia. Hydrogen transport through the ceramic is by means of protons rather than gaseous diffusion. Protons are introduced into the lattice when water vapour reacts with an oxygen ion vacancy at the surface by the hydration reaction (In Kröger-Vink notation),



One of the necessary requirements for ceramic proton conductors is gas-tightness against hydrogen. This places a new set of constraints on polycrystalline ceramic fabrication that goes well beyond the simple idea of "density". Ceramics processed by conventional means are often called dense, but fail the requirement for gas-tightness, particularly when thin membranes are used at elevated temperatures. This is because traditional sintering involves removal of the pores that form between adjacent ceramic grains during sintering. During intermediate-stage sintering, the dihedral pores actually form a series of interconnected channels that become easy paths for diffusion of molecular hydrogen and other gases. It is only during the final stage of sintering that the continuous pore channels are pinched off leaving a dihedral pore at each vertex of adjoining grains. These ideas are well-treated in many textbooks on ceramic sintering such as Barsoum [19]. Depending on the refractoriness of the ceramic material, these dihedral pores are nearly impossible to eliminate entirely, so the matter of ceramic density is more a qualitative determination of when the ceramic becomes "dense enough". It is the scattering of light from these pores that is the primary reason that oxide ceramics are typically opaque. Ceramic materials, such as magnesium aluminate spinel, can be made transparent with the use of sintering aids and high sintering pressures and temperatures, which effectively squeeze out the dihedral pores [20]. Transparency is a very good indication of high density. Even though "dense enough" in the case of ceramic membranes typically means that there are no pore channels that percolate through the matrix, the best evidence for density is transparency.

Barium zirconate is a very difficult-to-sinter material at reasonable temperatures. The refractoriness of barium zirconate is the main reason why adoption of the material as a ceramic proton conductor has been so slow. Techniques, such as hot isostatic pressing [21] and spark plasma sintering [21-23] have been explored with limited success. The most common approach to processing such materials is to begin with very high purity nanopowders prepared by sol-gel or spray pyrolysis methods [24-25]. This approach has worked well for fabricating

membranes dense enough for hydrogen separation applications, but fine-grained ceramic has more grain boundaries perpendicular to the direction of proton transport than coarse-grained ceramic. The core region between ceramic oxide grains in polycrystalline ceramics tend to become positively charged. This is not a problem for anion conductors, such as ZrO_2 and CeO_2 [26], but for proton conductors, the positive grain boundary charge serves to repel the positively charged protons, resulting in significant intrinsic grain boundary impedance [27-30]. Large grain size, on the other hand, extends the low temperature range where suitable operation is possible by decreasing the total grain boundary resistance.

For optimal proton conductivity it is desirable to obtain a ceramic microstructure with the largest possible grain size to reduce the effect of grain boundary impedance. Grain growth in barium zirconate during final-stage sintering is very slow, so simply sintering nanosized material for a longer time is not a viable option. Using micron-size calcined powders is also not an option. Traditionally, ceramic powder with the desired phase is prepared beforehand by solid-state reaction of the precursor oxides. This is how the ceramic powders were prepared for the sintered specimen shown in Fig. 1. Stoichiometric quantities of ZrO_2 , Y_2O_3 , and BaSO_4 were blended and reacted together in a covered crucible to make phase-pure $\text{BaZr}_{0.9}\text{Y}_{0.1}\text{O}_{3-d}$ (BZY10) powder, which was subsequently milled to about one micron size following the traditional method for preparing ceramic materials. Organic binder was added to the powder, pressed into a pellet under high pressure to ensure high green bulk density, and then sintered in air at $1650\text{ }^\circ\text{C}$ for up to 24 hours. It is obvious that ceramic prepared this way is not suitable for application as a hydrogen separation membrane.

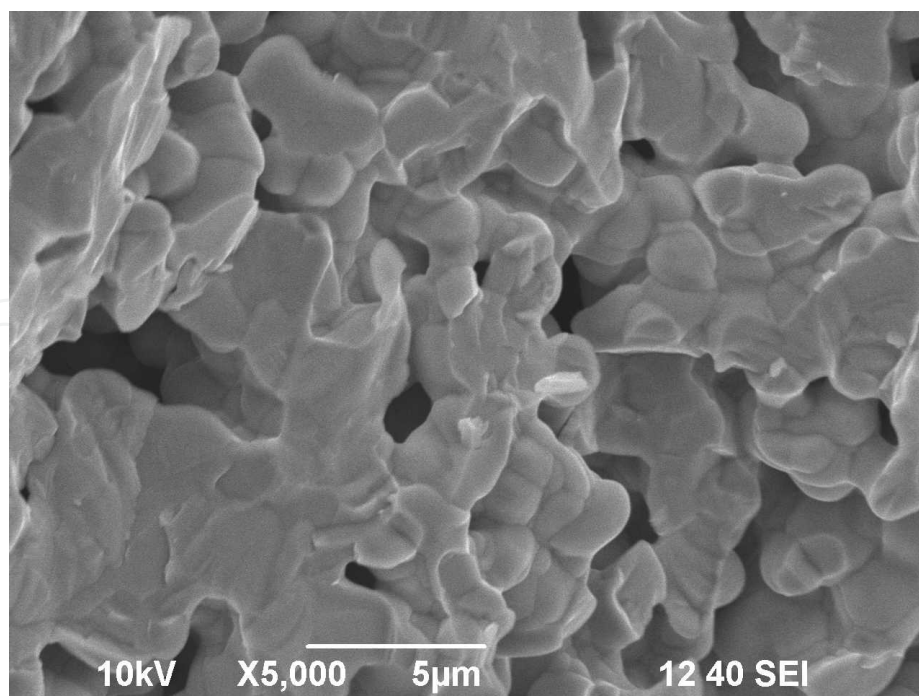


Figure 1. Poor sinterability of micron-size pre-calcined BZY10 powder at $1650\text{ }^\circ\text{C}$ for 24 hours in air (Courtesy of Wade Rosensteel, Colorado School of Mines).

An entirely new approach to fabrication of membrane quality barium zirconate ceramic, called solid-state reactive sintering (SSRS), has been developed [5-6, 31-33]. In this method the precursor powders are reacted and sintered in the same operation so that the perovskite phase is produced *in situ* and grain boundary movement never occurs. This results in large grain size and the absence of dihedral pores as shown in Fig. 2. This process will be explained in detail in Section 3.

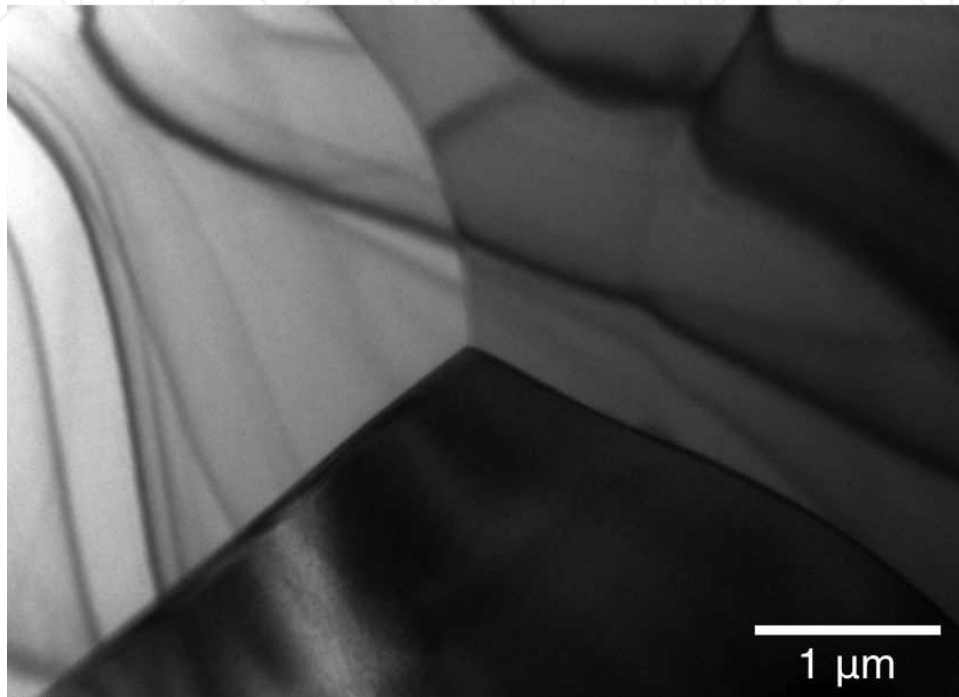


Figure 2. Low magnification bright-field TEM of dihedral in as-fired BaZr_{0.7}Ce_{0.2}Y_{0.1}O_{3-d} (Courtesy of Daniel Clark, Colorado School of Mines).

3. Solid state reactive sintering

3.1. Mechanism of the solid-state reactive sintering

The idea behind reactive sintering is quite simple. However, the ability to execute SSRS depends on identifying a glassy phase that consists of one of the components of the final desired ceramic phase. In the case of BZY, the A-site constituent, BaO, forms a binary eutectic glass with nickel oxide with a low melting point of 1125 °C. The BaO-NiO binary phase diagram is shown in Fig. 3. In solid-state reactive sintering, stoichiometric quantities of BaSO₄, ZrO₂, CeO₂ and Y₂O₃ are mixed together with a small amount of NiO – typically 0.1 wt% with organic binders to form a green body. During the initial heating cycle, NiO reacts with BaSO₄, releasing SO₂, and forming a liquid at the eutectic composition. As the temperature increases, ZrO₂ and Y₂O₃ begin to react together with Ba from the glass to form the more stable BZY perovskite phase. As more and more of the BZY phase forms, the BaO-NiO glass becomes increasingly

NiO rich, following the composition of the liquidus upwards to the right. Once the final sintering temperature is reached at about 1600 °C, the glass freezes at a composition of about 80-90% NiO and liquid phase sintering ceases. The last remaining Ba is extracted more slowly from the glass by solid-state diffusion and only NiO is left behind as a second phase [6].

As discussed in more details in Section 4.1., BaSO₄ is used instead of BaCO₃ because it is insoluble in water. Solid state reactive sintering can also be performed with BaCO₃.

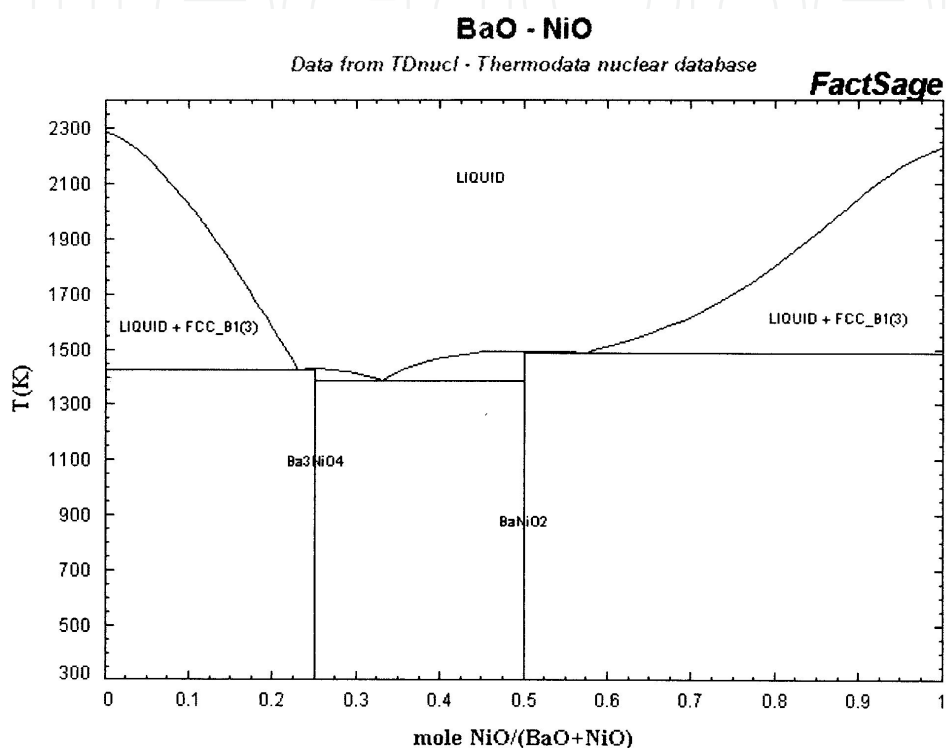


Figure 3. Binary phase diagram for BaO-NiO. (TDnucl – Thermodata nuclear database, FactSage).

The resulting BZY is phase pure, but the amount of residual NiO second phase, depends on the starting amount. Too much NiO leads to inclusions as shown in Fig. 4, but too little leads to incomplete BZY sintering. Ideally, there should be just enough NiO to coat the grain boundaries of the BZY phase with no more than about one monolayer of Ni atoms. Face centered cubic (FCC) NiO has a lattice parameter of 4.218 Å, which is a good match for BZY, 4.240 Å. It is straightforward to estimate the optimal amount of NiO if the BZY grains are treated as volume-filling truncated octahedra. The volume (V) of a 5 μm truncated octahedron is $8\sqrt{2} s^3$, where s is the side length ($3s$ is the side length of the regular octahedron). The distance between opposing square faces is $2\sqrt{2}s \approx 5 \mu\text{m}$. Therefore, $V = 62.5 \mu\text{m}^3$. The surface area of the same truncated octahedron is $A = (6+12\sqrt{2}) s^2 = 83.7 \mu\text{m}^2$. The thickness of one monolayer of NiO (body diagonal of the fcc lattice) is 0.6 nm, giving a volume of NiO of $0.05 \mu\text{m}^3$ per 5 μm BZY grain. The volume ratio is, thus, 0.08%. The density ratio of NiO to BZY is $6.67/6.16 = 1.08$, so the amount of NiO required to coat 5 μm BZY gains with a monolayer of NiO is slightly less than 0.1 wt%. Any more than this leads to inclusions, as shown in Fig. 4, and any less is

not sufficient to promote complete sintering. This calculation assumes that no NiO dissolves in the BZY crystallites. There is some evidence suggesting that NiO may enter the lattice as interstitial ions or even substitute on B-sites, but the amounts are negligible. Most of the NiO remains at grain boundaries. When just the right amount of NiO is used, the grain boundaries appear very clean, as shown in Fig. 5.

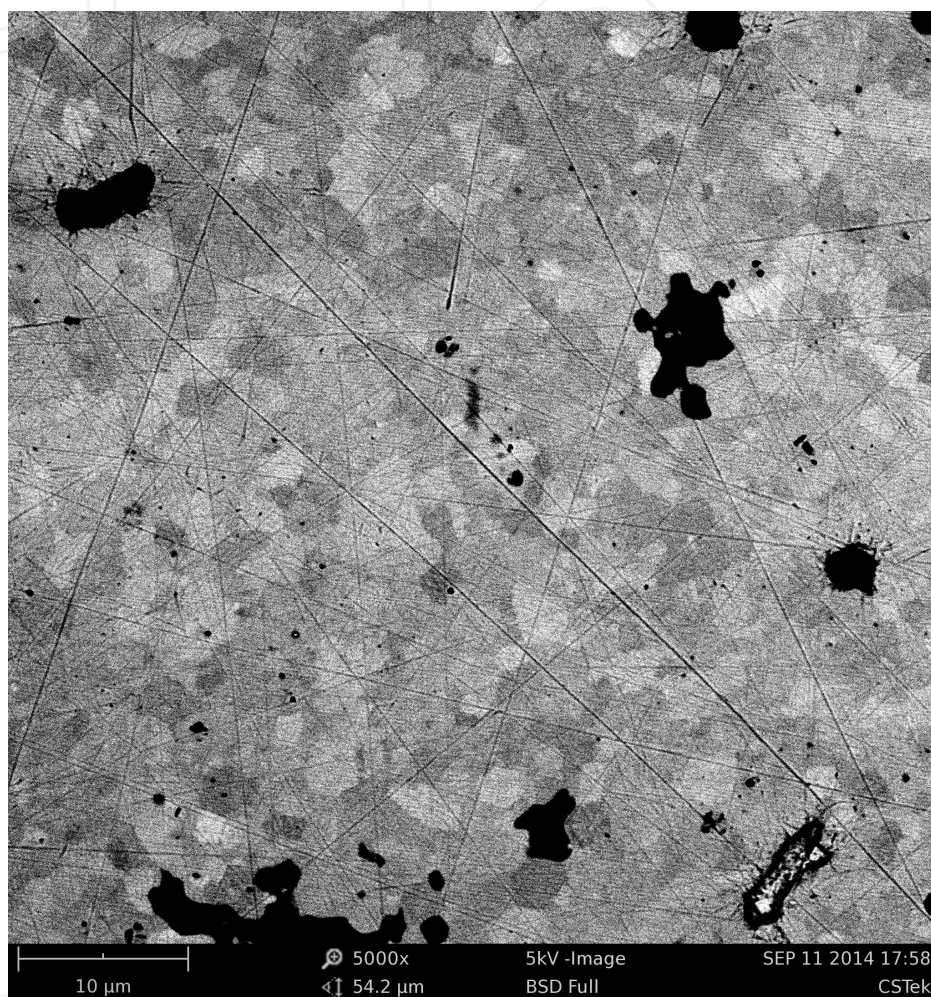


Figure 4. Back-scattered electron micrograph of polished BZY10 prepared by SSRS with 1 wt% NiO after specimen reduction. Dark regions are metallic nickel inclusions.

3.2. Ni nanoparticles

The small amount of NiO left behind at grain boundaries from SSRS has no practical effect as long as the ceramic is only exposed to oxidizing environments. But this defeats the purpose of a ceramic membrane intended for use in reducing atmosphere. When exposed to hydrogen at elevated temperatures, the NiO gets reduced. Upon reduction, metallic nickel nucleates along the grain boundaries and coarsens into nanoparticles that range in size from a few nanometers to 100 nm, depending on time and temperature. Fig. 6 shows the Ni-nanoparticles that form when a specimen of BZY prepared by SSRS with only 0.1 wt% NiO is annealed in hydrogen

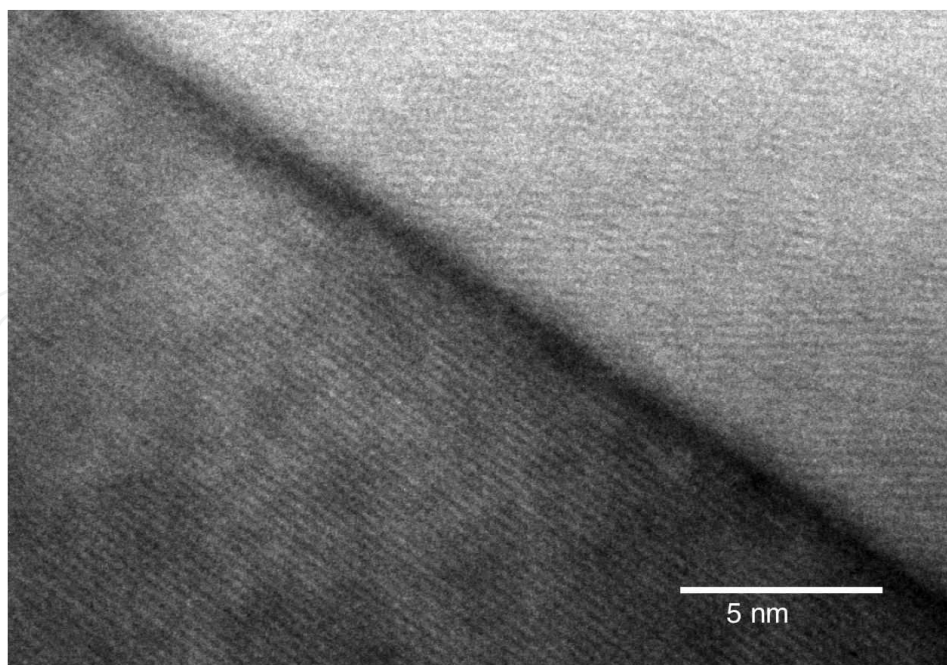


Figure 5. High resolution bright field TEM of as-fired $\text{BaZr}_{0.7}\text{Ce}_{0.2}\text{Y}_{0.1}\text{O}_{3-d}$ prepared by SSRS with 0.1 wt% NiO. Grain boundary region $\approx 5.8 \text{ \AA}$ (Courtesy of Daniel Clark, Colorado School of Mines).

at $1000 \text{ }^\circ\text{C}$ for 24 hours. It is interesting to note that the Ni-nanoparticles that grow on the crystal facets are all about the same size and uniformly distributed. This is reminiscent of star formation in a galaxy and provides clear evidence that the Ni-nanoparticles nucleated from a uniform coating of NiO between BZY grains. Using the calculation above for the volume of NiO per square micron of grain facet - $0.6 \times 10^6 \text{ nm}^3$ – the volume of equivalent Ni metal is about 75% or about $0.45 \times 10^6 \text{ nm}^3/\mu\text{m}^2$. A spherical 50 nm Ni particle has a volume of about $65,000 \text{ nm}^3$, so about 7 Ni nanoparticles per square micron of grain facet would be expected, which is about what is observed in Fig. 6.

One of the complications that arises in these protonic ceramic membranes is that the formation of Ni nanoparticles is irreversible. When the ceramic is exposed again to oxidizing conditions, rather than recoating the grain boundaries with a monolayer of NiO, the nanoparticles try to reoxidize in place, with a corresponding volume increase. This introduces local strain, which can lead to catastrophic failure. Fig. 7 shows the fracture that is characteristic of this condition. It is necessary to extract the NiO from the ceramic prior to reduction to levels below which fracture does not occur.

4. Nickel extraction

4.1. Specimen preparation

Barium zirconate and barium cerate can be reacted to make a complete solid solution over the entire composition range [4,6,9,14]. The most common nomenclature in use in the literature is

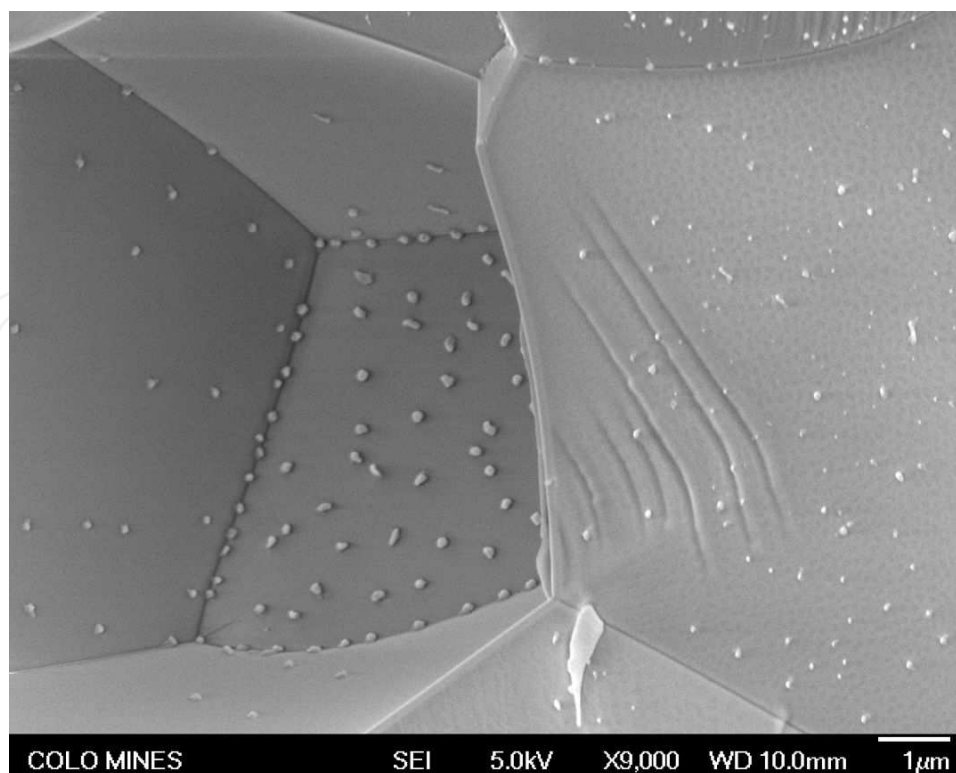


Figure 6. FESEM of Ni nanoparticles decorating grain boundary after reduction of $\text{BaZr}_{0.7}\text{Ce}_{0.2}\text{Y}_{0.1}\text{O}_{3-d}$ without NiO extraction heat-treatment.

BZCY mn , where m and n refer to the mole fractions of Zr and Ce on B-sites (times 10), respectively. For example, the formula for BZCY72 is $\text{BaZr}_{0.7}\text{Ce}_{0.2}\text{Y}_{0.1}\text{O}_{3-d}$. When there is no ceria, the common designation is BZY10, signifying 10 mol% yttrium. A small amount of ceria - up to 20 mol% - is advantageous in some cases. The material becomes chemically unstable in harsh environments for $\text{Ce} > 20$ mol% [34-35]. Furthermore, the electronic conductivity in dry hydrogen can be significant for $\text{Ce} > 10$ mol% [36]. In this monograph, the term, BZY, will be used for any ceramic formulation with more than 70 mol% Zr since structurally, there is practically no difference.

Solid state reactive sintering works with almost any ceramic green forming technique, so it is suitable for making everything from extruded tubes to cast tape. The method described here is for making 20 mm diameter by 1 mm thick discs by the time-honored method of slip casting. Slip casting is very easy and does not require expensive tooling. The discs are cast by simply filling PVC rings, arranged on a plaster-of-paris plate, with slip. The slip is prepared by mixing stoichiometric amounts of BaSO_4 , ZrO_2 , CeO_2 , and Y_2O_3 with additional 0.1 wt% NiO, DI water and conventional water-soluble, slip-casting binders. The reason for using BaSO_4 rather than BaCO_3 is that barium sulfate is insoluble in water. It is important in slip casting that no barium (or any cation) diffuse from the slip into the plaster-of-paris mold or base, thus altering the stoichiometry. Also, for health and safety reasons, it is inadvisable to use a water-soluble form of barium due to its toxicity. The slip is mixed in a Nalgene bottle on a jar roller for 2 hours with 10 mm zirconia balls. In reactive sintering, there is no need to adjust the particle size of

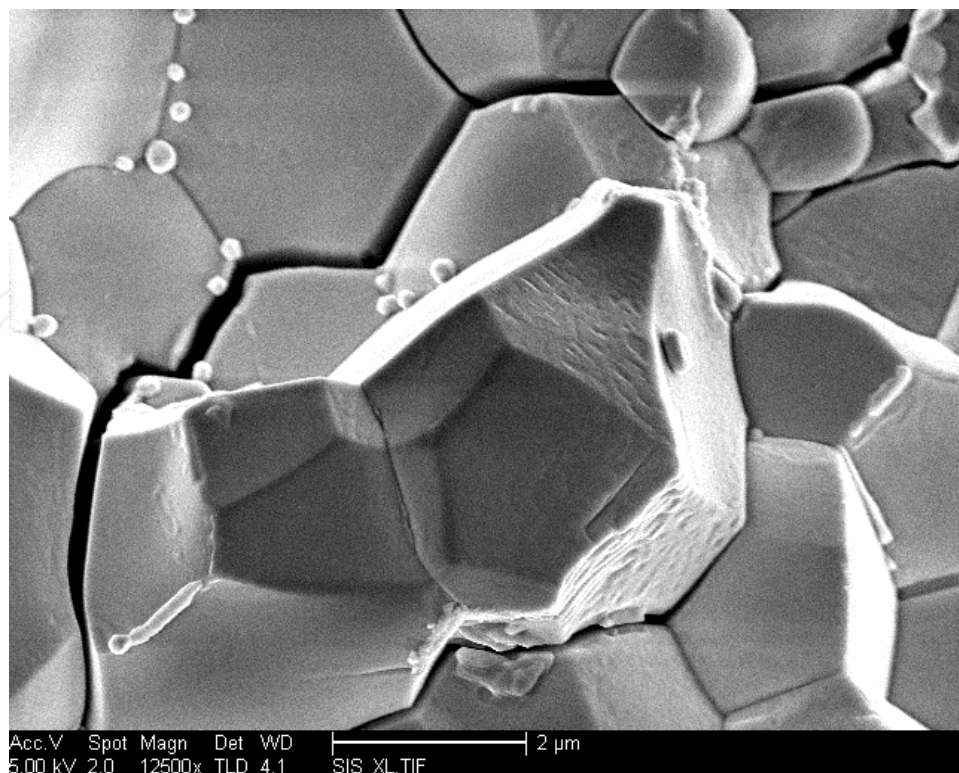


Figure 7. FESEM of intragranular fracture due to reoxidation of Ni nanoparticles in BZY10 (Courtesy of Thomas McGilvray, UCSD).

the precursor powders. It is sufficient just to obtain a homogeneous slip. The slip is filtered through a 325 mesh screen to remove the zirconia balls and any large agglomerates or undissolved binder, and continuously stirred prior to use to prevent settling.

Discs are cast by injecting a pre-calibrated amount of slip from a syringe into rings placed on a plaster-of-paris plate, and allowed to dry for several hours. Once dry and hard, the top surfaces of the cast discs are sanded flat to a thickness of about 3.5 mm. The discs are then stacked on top of BZY setters inside of a refractory enclosure to prevent excessive NiO loss during sintering. The initial sintering is carried out in air at 1600 °C for 16 hours. After sintering, the surfaces of the discs are ground with a diamond wheel on both faces to an overall thickness of 1.2 mm.

At this point in the process, the ceramic discs are fully dense and black. A second high temperature heat treatment is required to extract the NiO to a tolerable level. This is done by packing the ceramic in a bed of BZY powder inside of a ceramic retaining ring as shown in Fig. 8. A second firing cycle is carried out, also at 1600 °C. NiO extraction relies on relatively fast diffusion of NiO along grain boundaries until it reaches the surface of the specimen where it sublimates and is captured by the surrounding sacrificial BZY powder. The length of time required depends on the degree of extraction desired and the dimensions of the specimen. In the case of 1.2 mm thick discs, 16 hours is sufficient for achieving NiO level below 100 ppm. Fig. 9 shows a comparison of grain size distribution for the as-fired ceramic and after NiO extraction at 1600 °C for 16 hours. The grain-size measurements were carried out on powder

obtained by crushing the specimens, assuming that fracture occurred predominantly at grain boundaries. This is supported by the observation that the typical fracture surfaces of this material are predominantly inter-granular. The as-fired specimen experienced 16 hours at 1600 °C, whereas the NiO-extracted specimen effectively experienced 32 hours at this temperature. It may be observed that the average grain size increased only slightly, from 5 μm to 6.5 μm , demonstrating that grain growth during sintering in BZY is rather slow.

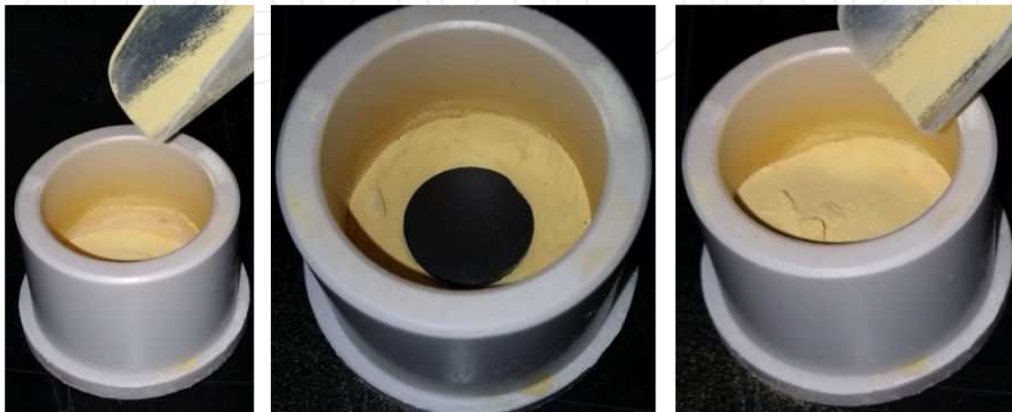


Figure 8. Set up for NiO extraction process. Center photo shows the black sintered disc placed on top of the BZY powder bed. Each part is covered with powder.

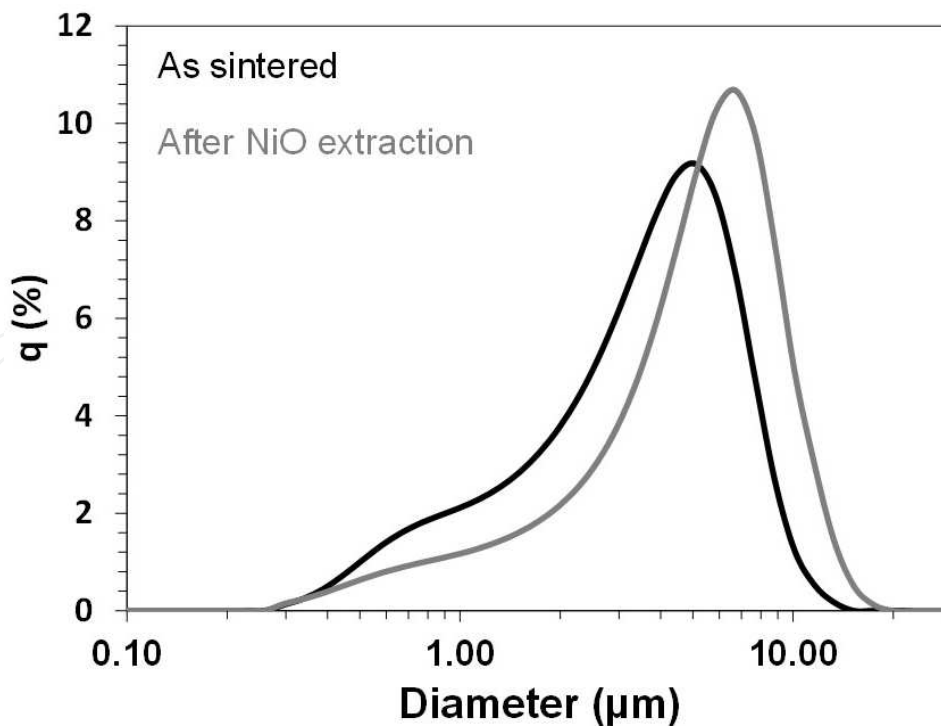


Figure 9. Grain size distributions of BZCY72 for as-fired (black) and after NiO extraction at 1600 °C for an additional 16 hours followed by an annealing treatment (grey) (Obtained with a Horiba Particle Size analyzer).

4.2. Characterization of the specimens after Ni extraction

4.2.1. Structural characterization

After the NiO extraction step, the discs are ground once more on both surfaces to the final 1.0 mm thickness, and ground on the outside diameter if necessary. A final annealing step in 4% H₂-bal Ar at 800 °C for 24 hours is carried out to condition the ceramic discs for the testing environment. Fig. 10 shows the appearance of two specimens, BZCY81 and BZCY72, after NiO extraction at 1600 °C, followed by annealing in H₂. The two specimens are transparent amber in color, and virtually Ni-free. Specimens with nickel extraction at only 1425 °C are dark and almost metallic-looking, demonstrating incomplete NiO extraction.



Figure 10. BZCY81 and BZCY72 specimens after NiO extraction at 1600 °C, followed by annealing in H₂ At 800 °C for 24 hrs.

XRD was used to ensure that the process of NiO extraction and subsequent annealing did not modify the BZY phase in any way. Five batches of specimens were prepared for this purpose: 1) As-fired, without NiO extraction or H₂ anneal, 2) NiO extraction only, 1425 °C for 16 hours, 3) NiO extraction, 1425 °C for 16 hours, plus H₂ anneal, 4) NiO extraction only, 1600 °C for 16 hours, and 5) NiO extraction, 1600 °C for 16 hours, plus H₂ anneal. The XRD patterns for $2\theta = 20$ to 120 degrees are shown in Fig. 11a. It may be observed that all cubic BZY peaks are present. The extra peak at $2\theta = 26.8$, present on all diffractograms, comes from small barium peroxide (ICDD file 00-007-0233). More significant is the finding in Fig. 11b where the (321) peaks are magnified. It may be observed that there is a very slight increase in the peak position with increasing NiO extraction. The cubic lattice parameter for as-fired material is 4.248 Å and that for the material after NiO extraction for 16 hours at 1600 °C is 4.245 Å, or 0.07% contraction. This could suggest that at least some of the NiO may have originated from the perovskite lattice, but it should be kept in mind that this change is much less than the change typically observed due to hydration and dehydration, so this conclusion is tenuous.

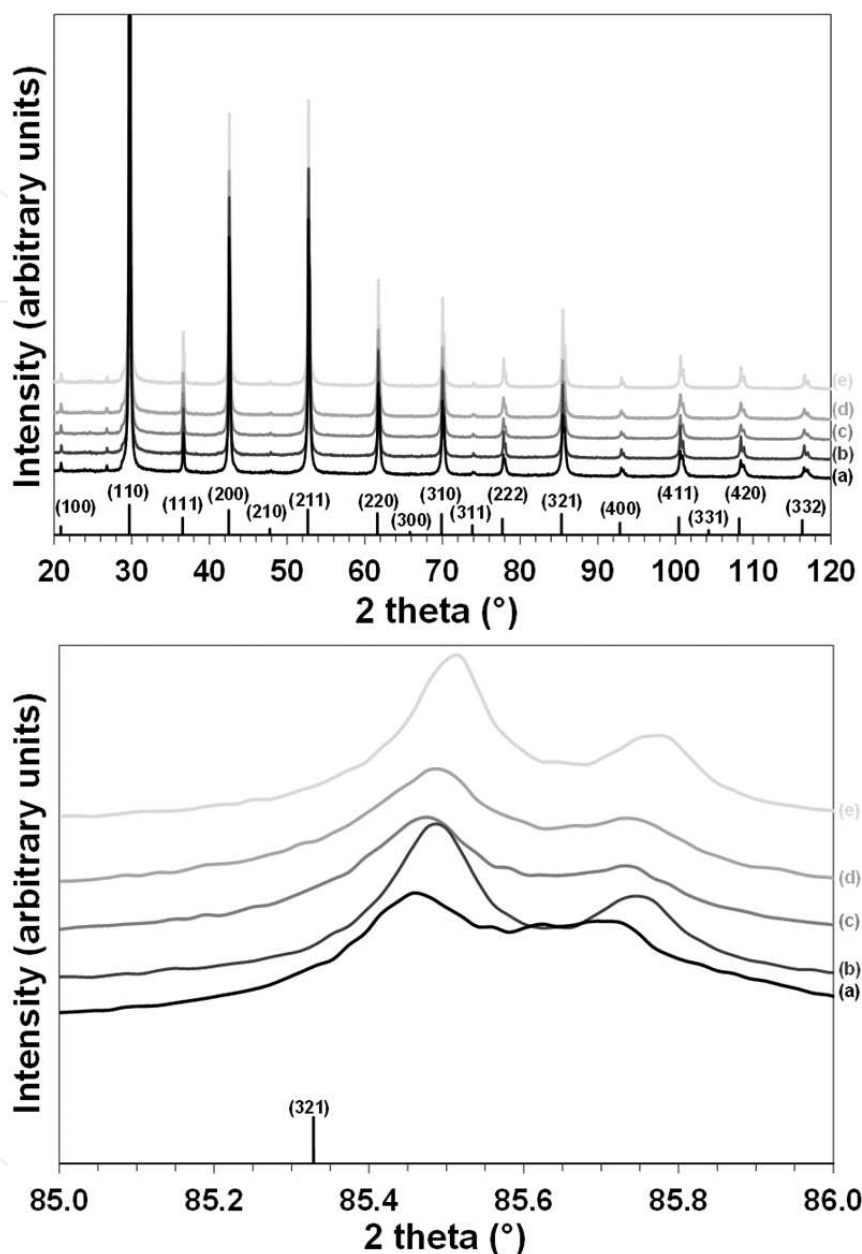


Figure 11. XRD of BZCY72 specimens prepared with different NiO extraction temperature. Full pattern (upper) and magnified (321) peak (lower). (a) as fired, (b) Ni extraction 16h 1475 °C, (c) Ni extraction 16h 1475 °C and annealed, (d) Ni extraction 16h 1600 °C, (e) Ni extraction 16h 1600 °C and annealed. The black bars correspond to the 04-011-7317 ICDD file.

After reduction in H_2 nearly all of the nickel may be assumed to be metallic, and ferromagnetic. This provides a convenient method for quantitative analysis of residual nickel content. It is extremely difficult to measure low levels of NiO reliably in sintered ceramics when the NiO is not uniformly distributed. By reducing the specimens, only metallic nickel remains, which can be quantitatively determined by magnetometry down to the parts per million lev-

el. A Quatum Design SQUID-based VSM with EverCool™ at 1.8 K to 400 K, oven temp of 1000 K, uniform field of 0.05 Oe to 70,000 Oe and magnetic moment, 10⁻⁸ emu to 10 emu, AC frequency: 0.1 Hz to 1000 H was used. Fig. 12 shows the magnetization plots after reduction in H₂ as a function of NiO extraction temperature (each for 16 hours); 1) 1425 °C, 2) 1550 °C and 3) 1600 °C. The estimate of the amount of Ni in the as-fired specimens was about 0.1 wt%. The NIST standard of 54.888 emu/g-Ni was used to determine the amount of Ni in the specimens at 5000 Oe. For example, the specimen with NiO extraction at 1475 °C had a magnetic moment of 0.022 emu/g-sample. Dividing this by 54.888 emu/g-Ni gives 0.039 wt % (times 58.69 g/mol-Ni/248.06 g/mol BZCY27 = 0.0092 mol%, or 92 ppm). Even at 92 ppm, the specimen was black and opaque. It was necessary to reduce the nickel to less than 0.002%, or about 4 ppm, in order to achieve transparency. It is seen that the extent of nickel extraction is highly dependent on NiO extraction temperature. Longer extraction times may be necessary for thicker specimens, but 1 mm is a good thickness for test specimens hydrogen flux measurements and electrode development.

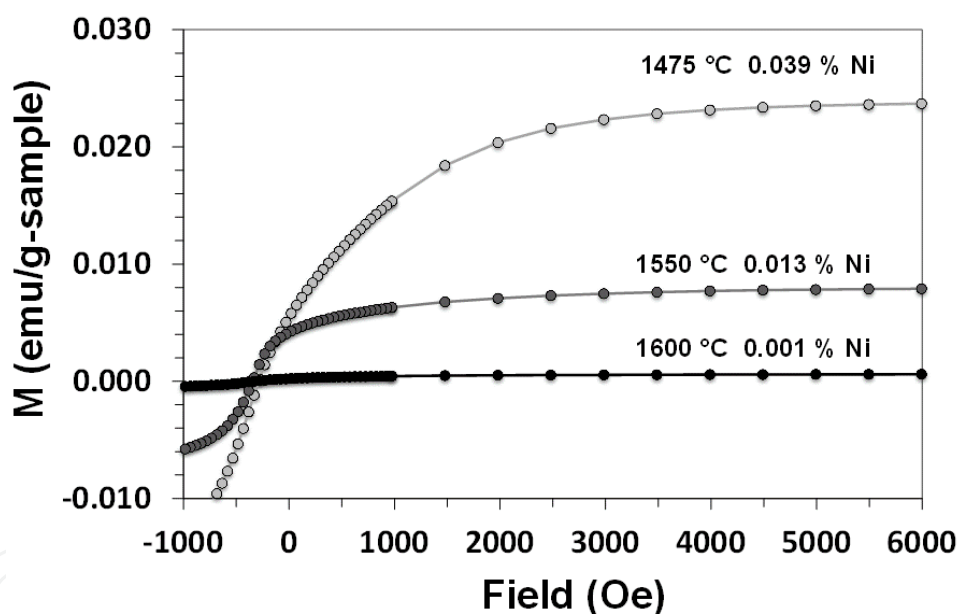


Figure 12. Magnetization curves for different NiO extraction temperatures. Ni concentrations calculated at 5000 Oe (0.5 Tesla) using NIST standard of 54.888 emu/g-Ni (courtesy of Jim O'Brien, UCSD).

4.2.2. Microstructural characterization

Back-scattered electron images on a polished BZCY72 specimen after Ni extraction and annealing in reducing atmosphere reveal the optimal microstructure: large grains (from 2 to 10 microns) with no dihedral pores and no Ni accumulation. An example is shown in Fig. 13. The grain boundaries of the specimen after nickel extraction and annealing in reducing atmosphere are free from nickel nano-particles (Fig. 14).

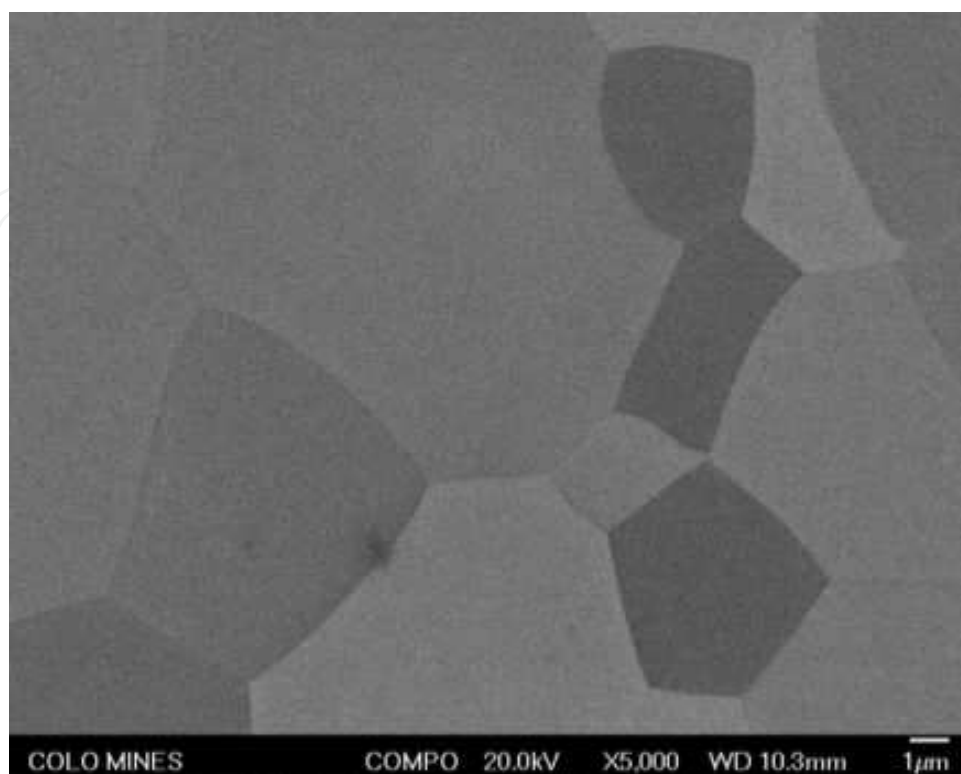


Figure 13. Back-scattered electron micrograph of a polished cross section of a BZCY72 ($\text{BaZr}_{0.7}\text{Ce}_{0.2}\text{Y}_{0.1}\text{O}_{3-d}$) after Ni extraction (16h 1600 °C) and annealing in reducing atmosphere.

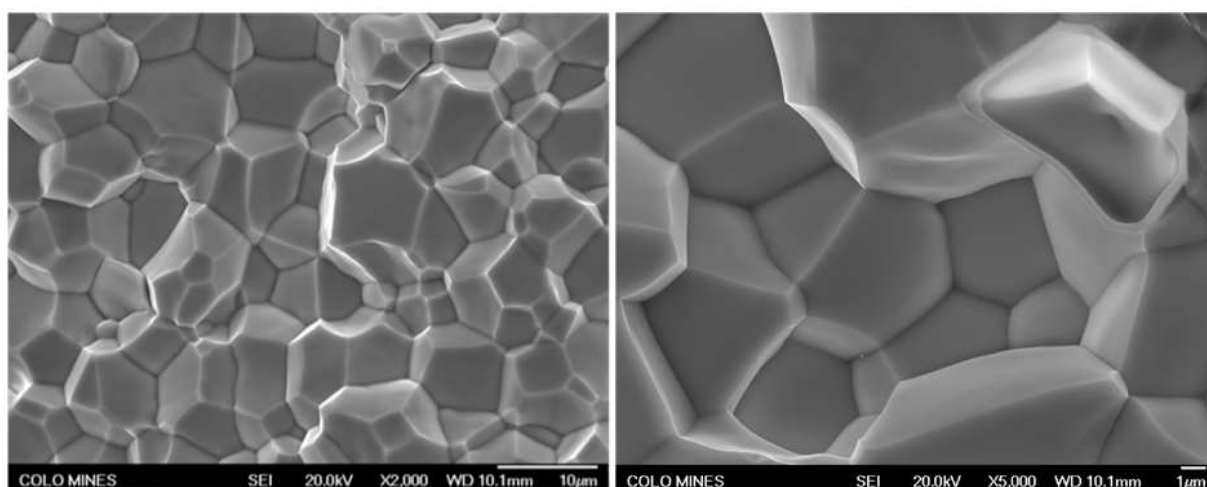
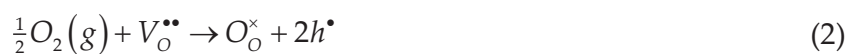


Figure 14. Secondary electron micrographs of a fractured cross-section of a BZCY72 ($\text{BaZr}_{0.7}\text{Ce}_{0.2}\text{Y}_{0.1}\text{O}_{3-d}$) after Ni extraction (16h 1600 °C) and annealing in reducing atmosphere.

4.2.3. Electronic characterization

In moist atmosphere, BZY materials incorporate protonic defects (OH_O^\bullet) in their lattice according to Eq. 1. For such a reaction to happen, oxygen vacancies are necessary. Some ceramic proton-conductors, such as pyrochlores [37-38], have intrinsic oxygen vacancies. For barium zirconate based materials, the oxygen vacancies are extrinsically created by substituting the B-site of the perovskite (4+) by a trivalent cation (most commonly yttrium). Once in the lattice, the protonic defects diffuse according to the Grotthuss mechanism [39]. The protons are the only mobile species while the oxygen is localized in the vicinity of its crystallographic position [3].

In oxidizing atmosphere, oxygen dissociates in the oxygen vacancies. The corresponding reaction is most of the time reported as equation (2) [40-43], which can be misleading because the electron holes are not valence holes. Indeed, in models, these electron holes are treated as localized, since the Nernst Einstein equation is used [44]. However, no localization is defined. To avoid confusion, equation 2 can be rewritten as equation 3, assuming the electron holes are localized on the O-site [45-46].



The conductivity was measured on 1 mm-thick pellets prepared as described in section 3.1 but with a smaller diameter (13 mm). Pt electrodes were painted on both sides of the pellet and fired in air for 30 min at 1000 °C. Impedance spectra were recorded from 20 Hz to 1 MHz using Hewlett Packard 4284A Precision LCR Meter interfaced with Labview and were fitted using the Zsimpwin software. The oxygen partial pressure dependences of the conductivity, with an example for BZCY72 in Fig. 15, exhibit the typical behavior for a BZY material in moist atmosphere:

- A plateau at oxygen partial pressure below 10^{-5} atm, which corresponds to the ionic conductivity. It is agreed that for BZY material, the ionic conductivity is mainly protonic at temperature below 700 °C [47-48],
- An increase of the conductivity with the oxygen partial pressure in oxidizing atmosphere, from the incorporation of the oxygen (Eq. 3).

According to Fig. 15, the protonic conductivity of the BZCY72 specimens after Ni extraction is 2.5 and 1.3 mS.cm⁻¹ at 700 and 600 °C respectively. These values are consistent with those reported in the literature for BZCY72 [9,32,34-35,49], indicating that the extraction process did not deteriorate the specimens.

Some electronic conductivity in reducing atmosphere was measured in barium cerate based materials [50-51], generating from the reduction of the cerium cations and the formation of

small polarons. In the present work, the conditions were not reducing enough to generate cerium small polarons. However, this phenomenon has been observed on thin BZCY72 membranes [36]. Depending on the desired operation (gas composition, humidification rate and temperature), the percentage of cerium needs to be adjusted.

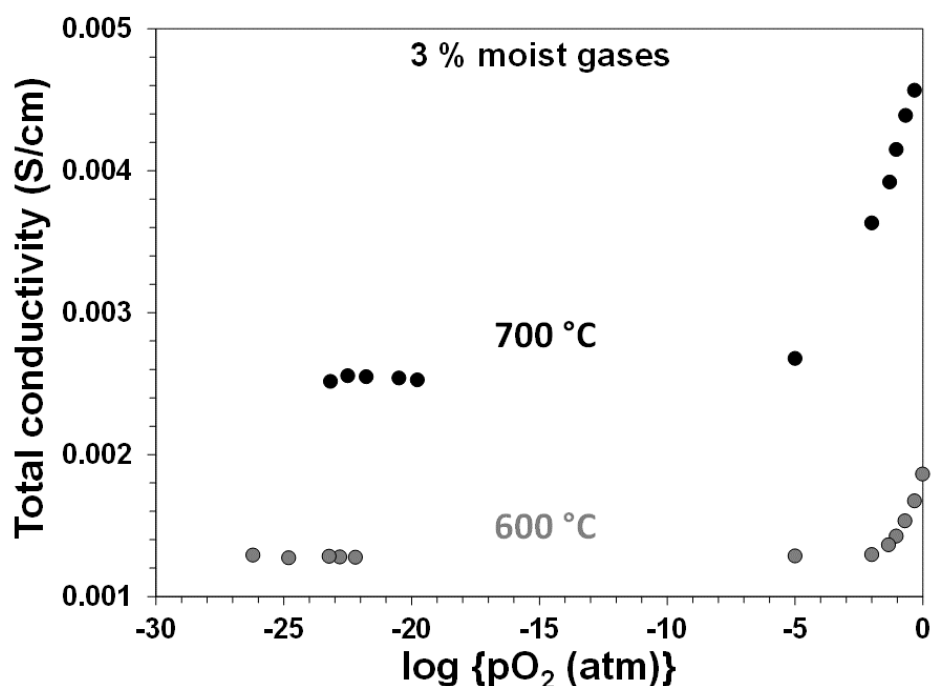


Figure 15. pO₂ dependence of the conductivity measured on a BZCY27 pellet after Ni extraction.

As mentioned in the introduction, the high grain-boundary resistivity in the BZY materials has been explained by the presence of a space-charge layer [27-30]. The width and the magnitude of the space-charge layer depends on the synthesis/sintering processes [52]. The grain-boundary contribution to the conductivity can be decreased by having a large grain microstructure. Indeed, the larger the grains, the smaller the grain boundary density. But other factors, such as the dopant accumulation, the barium evaporation or the segregation of impurities at the grain-boundary, play an important role in the space-charge layer.

The conductivity was recorded as a function of temperature in 3% moist 5% H₂, balance Ar. At high temperature, the spectra were fitted with 2 (RQ) elements in series, with R, a resistance and Q, a constant phase element. The different processes could be analyzed using the pseudo-capacitance. The first (RQ) was assigned to the bulk (~10⁻¹¹ F) and the second one to the Pt electrodes (~10⁻⁶ F). With decreasing temperature, the grain-boundary contribution becomes visible. Because of the frequency range used for the measurement, the electrode contribution does not appear anymore at low temperature (lower frequencies would be needed). Therefore, at low temperature, the spectra were also fitted with two (RQ) in series, the first one for the bulk and the second one for the grain boundaries (~10⁻⁹ F). Example of the fits of the impedance spectra at 600 and 400 °C are displayed in Fig. 16. The Arrhenius plot of the conductivity in

3% moist 5% H₂, balance Ar, cf. Fig. 17, gives an activation energy for proton diffusion of 0.47 eV for the bulk and 0.78 eV for the grain-boundaries. Similar values were reported in the literature [13,28,30,52].

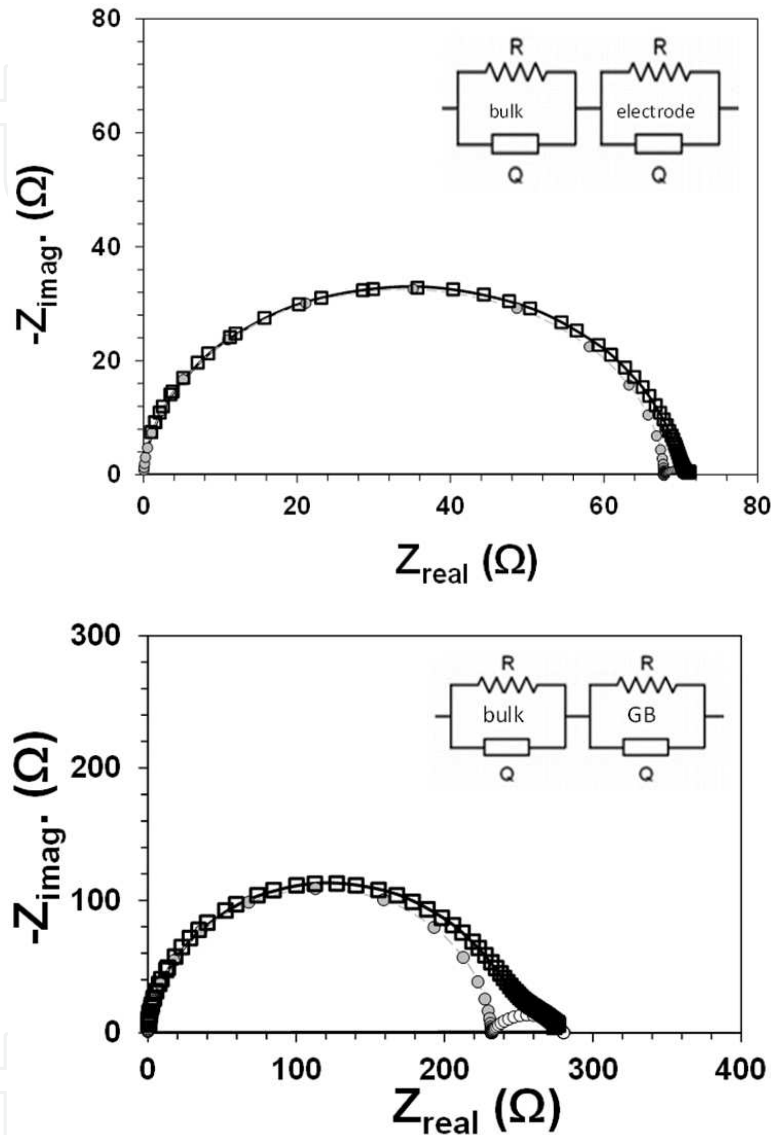


Figure 16. Impedance spectra of BZCY72 after Ni extraction in 3% moist 5% H₂, balance Ar. (upper) 600 °C and (lower) 400 °C. GB stands for grain boundary

5. Summary

A process has been described for making dense, large-grained BZY suitable for use in hydrogen diffusion membranes. It is nearly impossible to make meaningful measurements on membranes films, themselves, on the order of tens of microns thick. The thick specimens shown in Fig. 10 are intended for testing purposes, where it is desirable to have

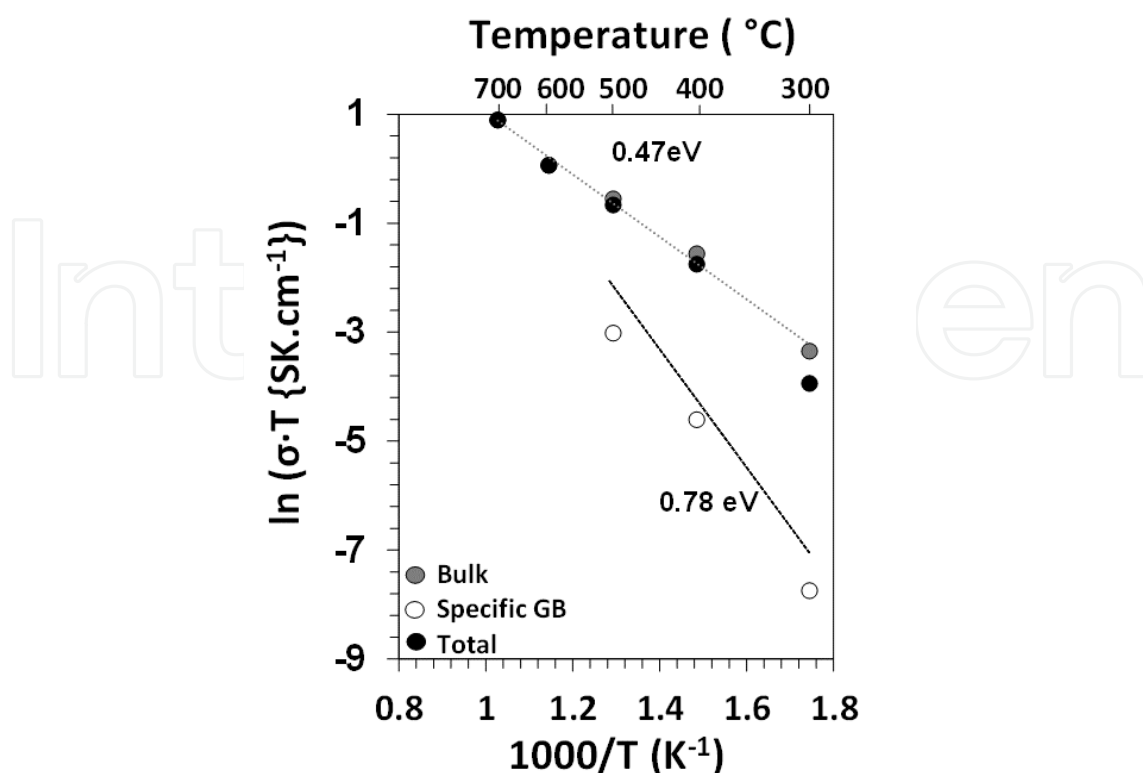


Figure 17. Arrhenius plot for BZCY72 after Ni extraction in 3% moist 5% H₂, balance Ar. The specific grain-boundary (GB) conductivity is obtained by multiplying the grain-boundary conductivity by the ratio of the pseudo-capacitance of the bulk over the pseudo-capacitance of the grain boundaries [53].

ceramic material that is representative of thin membranes for such things as electrode development, measurement of bulk mechanical and electrical properties, etc. The fact that the specimens are transparent is incidental, except that this unique property makes it possible to measure bulk optical properties, such as band gap, by transmission spectra (see Chapter 16 of Fundamentals of Ceramics [19]).

Practical hydrogen diffusion membranes must be as thin as possible in order to maximize the hydrogen flux, but still remain impervious to all other gas species. Fig. 18 shows the cross-section of a typical BZCY72 membrane coating on a porous support tube for a protonic ceramic fuel cell or membrane reactor from a 10 mm diameter production tube from CoorsTek Membranes Sciences. The 20 μm-thick membrane is shown in the upper part of the image coating a 0.8 mm thick Ni/BZCY72 anode-support. The image was obtained on a polished specimen that highlights the microstructure. The fully dense and large-grained microstructure of the membrane is clearly seen. Such a membrane is capable of passing a hydrogen flux of about 5 μmol/cm².s (7.3 nml/min/cm²) from a H₂/He permeant stream at 700 °C while passing negligible detectable helium, as determined by analysing the permeate by mass spectrometry.

Solid-state reactive sintering is a very robust and cost effective method for making such membranes on the scale of hundreds of millions of square meters that will be required for commercialization of this technology.

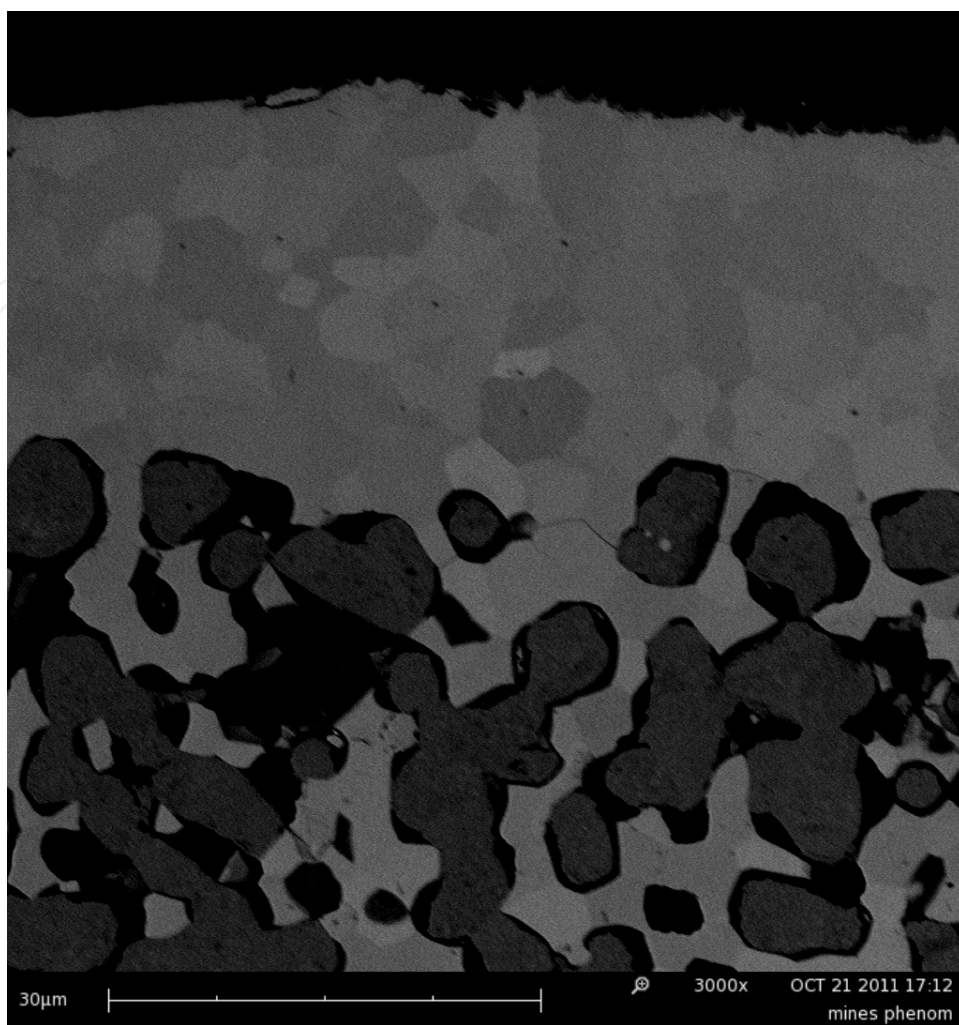


Figure 18. Polished cross-section of BZCY72 membrane on porous Ni/BZCY72 cermet support.

Acknowledgements

The authors acknowledge Daniel Clark from Colorado School of Mines for the transmission electron micrograph, Dr. Jim O' Brien for providing the Squid Data, Mc Gilvray at UCSD for FESEM and Dr. Grant Hudish at CoorsTek for collecting the XRD data.

Author details

W. Grover Coors¹, Anthony Manerbino¹, David Martinefski¹ and Sandrine Ricote²

¹ CoorsTek, Inc. Golden, Colorado, USA

² Colorado School of Mines, Golden, Colorado, USA

References

- [1] Iwahara H, Eska T, Uchida H, Maeda N (1981) Proton Conduction in Sintered Oxides and its Application to Steam Electrolysis for Hydrogen Production. *Solid State Ionics* 3/4:359-363.
- [2] Slade RT (1989) Preface to the Special Proceedings of the 4th International Conference on Solid State Proton Conductors. *Solid State Ionics* 35.
- [3] Kreuer KD (1999) Aspects of the formation and mobility of protonic charge carriers and the stability of perovskite-type oxides. *Solid State Ionics* 125:2085-302.
- [4] Ryu KH, Haile SM (1999) Chemical stability and proton conductivity of doped Ba-CeO₃-BaZrO₃ solid solutions. *Solid State Ionics* 125:355-367.
- [5] Babilo P, Haile SM (2005) Enhanced sintering of yttrium-doped barium zirconate by addition of ZnO. *J. Am. Ceram. Soc.* 88:2362-2368.
- [6] Coors WG (2011) Co-ionic Conduction in Protonic Ceramics of the Solid Solution, BaCe_xZr_(y-x)Y_(1-y)O_{3-d}; Part I: Fabrication and Microstructure. In: Sikalidis C, editor. *Ceramic Materials Book 3*. Intech. pp.479-500.
- [7] Kreuer KD (2003) Proton-conducting oxides. *Annu. Rev. Mater. Res.* 22:333-359.
- [8] Babilo P, Uda T, Haile SM (2007) Processing of yttrium-doped barium zirconate for high proton conductivity. *J. Mater. Res.* 22:1322-1330.
- [9] Katahira K, Kohchi Y, Shimura T, Iwahara H (2000) Protonic conduction in Zr-substituted BaCeO₃. *Solid State Ionics*. 138:91-98.
- [10] Schober T, Bohn HG (2000) Water vapor solubility and electrochemical characterization of the high temperature proton conductor BaZr_{0.9}Y_{0.1}O_{2.95}. *Solid State Ionics* 127:351-360.
- [11] Tao S, Irvine JTS (2007) Conductivity studies of dense yttrium-doped BaZrO₃ sintered at 1325°C. *J. Solid State Chem.* 180:3493-3503.
- [12] Pergolesi D, Fabbri E, Traversa E (2012) Chemically stable anode-supported solid oxide fuel cells based on Y-doped barium zirconate thin films having improved performance. *Electrochemistry Communications* 12:977-980.
- [13] Duval SBC, Holtappels P, Vogt UF, Stimming U, Graule T (2010) Characterisation of BaZr_{0.9}Y_{0.1}O_{3-d} Prepared by Three Different Synthesis Methods: Study of the Sinterability and the Conductivity. *Fuel Cells* 5:312-321.
- [14] Ricote S, Bonanos N, Marco De Luca MC, Caboche G (2009) Structural and conductivity study of the proton conductor BaCe_{0.9-x}Zr_xY_{0.1}O_{3-d}. *J. Power Sources* 193:189-193.
- [15] Stotz VS, Wagner C (1960) Die Löslichkeit von Wasserdampf und Waeserstoff in festen Oxiden. *Ber Bunsenges Phys Chem.* 70:781-788.

- [16] Bonanos N (1992) Transport properties and conduction mechanism in high-temperature protonic conductors. *Solid State Ionics*. 53-56:967-974.
- [17] Kosacki I, Tuller HL (1995) Mixed conductivity in $\text{SrCe}_{0.95}\text{Yb}_{0.05}\text{O}_3$, protonic conductors. *Solid State Ionics*. 80:223-229.
- [18] Krug F, Schober T, Springer T (1995) In situ measurements of the water uptake in Yb doped SrCeO_3 . *Solid State Ionics* 81:111-118.
- [19] Barsoum MW (2003) Sintering and grain growth. In: Taylor & Francis Group. *Fundamentals of Ceramics*. LLC. pp. 302-354.
- [20] Meir S, Kalabukhov S, Froumin N, Dariel MP, Frage N (2009) Synthesis and Densification of Transparent Magnesium Aluminate Spinel by SPS Processing. *J. Am. Ceram. Soc.* 92:358-364.
- [21] Dahl PI, Lein HL, Yu Y, Tolchard J, Grande T, Einarsrud M-A, Kjølseth C, Norby T, Haugrud R (2011) Microstructural characterization and electrical properties of spray pyrolyzed conventionally sintered or hot-pressed BaZrO_3 and $\text{BaZr}_{0.9}\text{Y}_{0.1}\text{O}_{3-\delta}$. *Solid State Ionics* 182:32-40.
- [22] Anselmi-Tamburini U, Buscaglia MT, Viviani M, Bassoli M, Bottino C, Buscaglia V, Nanni P, Munir ZA (2006) Solid-state synthesis and spark plasma sintering of submicron $\text{BaY}_x\text{Zr}_{1-x}\text{O}_{3-x/2}$ ($x = 0, 0.08$ and 0.16) ceramics. *J. European Ceram. Soc.* 26:2313-2318.
- [23] Ricote S, Bonanos N, Wang HJ, Boukamp BA (2012) Conductivity study of dense $\text{BaZr}_{0.9}\text{Y}_{0.1}\text{O}_{3-\delta}$ obtained by spark plasma sintering. *Solid State Ionics* 213:36-41.
- [24] Barison S, Battagliarin M, Cavallin T, Doubova L, Doubova M, Mortalo C, Boldrini S, Malavasi L, Gerbasi R (2008) High conductivity and chemical stability of $\text{BaCe}_{1-x-y}\text{Zr}_x\text{Y}_y\text{O}_{3-d}$ proton conductors prepared by a sol-gel method. *J. Mater. Chem.* 18:5120-5128.
- [25] Stuart PA, Unno T, Ayres-Rocha R, Djurado E, Skinner SJ (2009) Synthesis and sintering behaviour of BaZrYO_3 powders prepared by spray pyrolysis. *J. European Ceram. Soc.* 29:697-702.
- [26] Kim S, Fleig J, Maier J: Space charge conduction (2003) Simple analytical solutions for ionic and mixed conductors and application to nanocrystalline ceria. *Phys. Chem. Chem. Phys.* 5:2268-2273.
- [27] Iguchi F, Sata N, Yugami H (2010) Proton transport properties at the grain boundary of barium zirconate based proton conductors for intermediate temperature operating SOFC. *J. Mater. Chem.* 20:6265-6270.
- [28] Kjølseth C, Fjeld H, Prytz Ø, Dahl PI, Estournes C, Haugrud R, Norby T (2010) Space-charge theory applied to the grain boundary impedance of proton conducting $\text{BaZr}_{0.9}\text{Y}_{0.1}\text{O}_{3-\delta}$. *Solid State Ionics* 181:268-275.

- [29] Chen CT, Danel CE, Kim S (2011) On the origin of the blocking effect of grain-boundaries on proton transport in yttrium-doped barium zirconates. *J. Mater. Chem.* 21:5435-5442.
- [30] Shirpour M, Merkle R, Maier J (2012) Evidence for space charge effects in Y-doped BaZrO₃ from reduction experiment. *Solid State Ionics.* 216:1-5.
- [31] Tong J, Clark D, Hoban M, O'Hayre R (2010) Cost-effective solid-state reactive sintering method for high conductivity proton conducting yttrium-doped barium zirconium ceramics. *Solid State Ionics* 181:496-503.
- [32] Ricote S, Bonanos N, Manerbino A, Coors WG (2012) Conductivity study of dense BaCe_xZr_{0.9-x}Y_{0.1}O_{3-d} prepared by solid state reactive sintering at 1500°C. *International J. Hydrogen Energy* 37:7954-7961.
- [33] Fang S, Wang S, Brinkman KS, Chen F (2014) A sinteractive Ni-BaZr_{0.8}Y_{0.2}O_{3-d} composite membrane for hydrogen separation. *J. Mater. Chem.* 2:5825-5833.
- [34] Zong Z (2007) Stability and conductivity study of the BaCe_{0.9-x}Zr_xY_{0.1}O_{2.95} systems. *Solid State Ionics* 178:213-220.
- [35] Ricote S, Bonanos N, Caboche G (2009) Water vapour solubility and conductivity study of the proton conductor BaCe_(0.9-x)Zr_xY_{0.1}O_(3-d). *Solid State Ionics* 180:990-997.
- [36] Babiniec SM, Ricote S, Sullivan NP (2015) Characterization of ionic transport through BaCe_{0.2}Zr_{0.7}Y_{0.1}O_{3-d} membranes in galvanic and electrolytic operation. *International J. Hydrogen Energy* 40: 9278–9286.
- [37] Subramanian MA, Aravamudan G, Rao GVS (1983) Oxide pyrochlores –a review. *Progress in Solid State Chemistry* 15:55-143.
- [38] Besikiotis V, Ricote S, Hjorth Jensen M, Norby T, Haugrud R (2012) Conductivity and hydration trends in disordered fluorite and pyrochlore oxides: A study on lanthanum cerate–zirconate based compounds. *Solid State Ionics* 279:26-32.
- [39] Agmon N (1995) The Grotthuss mechanism. *Chem. Phys. Letters* 244:456-462.
- [40] Norby T, Larring Y (2007) Concentration and transport of protons in oxides. *Current Opinion in Solid State & Materials Science* 2:593-599.
- [41] Poulsen FW (1999) Method for calculating ionic and electronic defect concentrations in proton containing perovskites. *J. Solid State Chem.* 143:115-121.
- [42] Schober T, Schilling W, Wenzl H (1996) Defect model of proton insertion into oxides. *Solid State Ionics* 86-88:653-658.
- [43] Uchida H, Maeda N, Iwahara H (1983) Relation between proton and hole conduction in SrCeO₃-based solid electrolytes under water containing atmospheres at high temperatures. *Solid State Ionics* 11:117-124.
- [44] Oishi M, Akoshima S, Yashiro K, Sato K, Mizusaki J, Kawada T (2008) Defect structure analysis of B-site doped perovskite-type proton conducting oxide BaCeO₃ Part 2:

The electrical conductivity and diffusion coefficient of $\text{BaCe}_{0.9}\text{Y}_{0.1}\text{O}_{3-\delta}$. *Solid State Ionics* 179:2240-2247.

- [45] Stokes SJ, Islam MS (2010) Defect chemistry and proton-dopant association in BaZrO_3 and BaPrO_3 . *J. Mater. Chem.* 20:6258-6264.
- [46] Hermet J, Bottin F, Dezanneau G, Geneste G (2012) Thermodynamics of hydration and oxidation in the proton conductor Gd-doped barium cerate from density functional theory calculations. *Physical review B* 85:205137 1-14
- [47] Iwahara H (1995) Technological challenges in the application of proton conducting ceramics. *Solid State Ionics* 77:289-298.
- [48] Ricote S, Bonanos N, Wang HJ, Haugrud R (2011) Conductivity, transport number measurements and hydration thermodynamics of $\text{BaCe}_{0.2}\text{Zr}_{0.7}\text{Y}_{(0.1-\xi)}\text{Ni}_\xi\text{O}_{(3-\delta)}$. *Solid State Ionics* 185:11-17.
- [49] Fish JS, Ricote S, O'Hayre R, Bonanos N (2014) Electrical properties and flux performance of composite ceramic hydrogen separation membranes. *J. Mater. Chem. A.* 3:5392-5401.
- [50] He T, Kreuer KD, Baikov Yu.M, Maier J (1997) Impedance spectroscopic study of thermodynamics and kinetics of a Gd-doped BaCeO_3 single crystal. *Solid State Ionics* 95:301-308.
- [51] Bonanos N (1993) Transport study of the solid electrolyte $\text{BaCe}_{0.9}\text{Gd}_{0.1}\text{O}_{2.95}$ at high temperatures. *J. Phys. Chem. Solids* 54:867-870.
- [52] Ricote S, Bonanos N, Manerbino A, Sullivan NP, Coors WG (2014) Effects of the fabrication process on the grain-boundary resistance in $\text{BaZr}_{0.9}\text{Y}_{0.1}\text{O}_{3-d}$. *J. Mater. Chem. A.* 2:16107-16115.
- [53] Haile SM, Staneff G, Ryu KH (2001) Non-stoichiometry, grain-boundary transport and chemical stability of proton conducting perovskites. *J. Materials Science* 36:1149-1160.